P. Wang
Department of Renewable Energy,
Hohai University,
Nanjing 210029, China;
Department of Mechanical Engineering,
University of California,
Riverside, CA 92521

K. Vafai[1]
Fellow ASME
Department of Mechanical Engineering,
University of California,
Riverside, CA 92521
e-mail: vafai@engr.ucr.edu

Modeling and Analysis of an Efficient Porous Media for a Solar Porous Absorber With a Variable Pore Structure

A theoretical mathematical model that considers the continuous linear porosity or pore diameter distribution is established to develop a novel porous absorber with variable pore structure, which will result in a thermopressure drop improvement. Efficient performance can be achieved based on reconstruction of the velocity, temperature, and radiation fields. Collimated and diffusive radiative heat fluxes and the heat loss mechanism from the irradiated surface are analyzed in the presence of the volumetric effect. This study analyzes three typical linear pore structure distributions: increasing (I), decreasing (D), and constant (C) types, respectively. In general, the D type porosity (φ) layout combined with the I type pore diameter (d_p) distribution would be an excellent pore structure layout for a porous absorber. [DOI: 10.1115/1.4037161]

Keywords: variable pore structure, modeling, thermal efficiency, pressure drop, solar absorber

1 Introduction

Despite various designs, all the receivers can be divided into two types according to the basic heat transfer element of the absorber, which is either tubular or volumetric. With the gas tubular absorber, the glass window is easily maintained due to the free pressure receiver design [1]. Theoretically, higher temperatures can be reached; however, the limiting factor is a low heat transfer coefficient [2].

Roldán et al. [3] studied and experimented with the heat transfer processes of a cavity solar furnace and the data were compared with the numerical simulation results. A computational model has been developed to study the influence of wind and the effect of return-air conditions on the efficiency of a previously tested volumetric receiver [4]. Some in-house numerical research has also been carried out. Cheng et al. [5] coupled the heliostat field with the windowed volumetric solar receiver (VSR) using the developed Monte Carlo ray tracing code. The optical efficiency of the heliostat field and the local heat flux distribution within the silicon carbide (SiC) absorber is calculated, and the same method is applied to a cylinder VSR in a dish system [6]. Furthermore, Fend et al. developed a flow-scheme and temperature distribution of a modular single cup absorber [7]. The influence on the temperature distribution and efficiency from slight geometric changes to the absorber was then analyzed. A solar receiver integrated with a small-scale (10 kWel) gas turbine system has been designed with a special focus on the tradeoffs between efficiency, pressure drop, material utilization, and economic considerations [8].

The critical advantage of the VSRs derives from the heat-resistant porous absorber (over 1300 °C) under the "volumetric effect," the pore structure enhancement of radiative energy transfer into a vertical channel was analyzed in an earlier work [9]. We also presented a unified theoretical model [10] in a windowed VSR as well as a small-scale experiment [11] to validate the model. Some researchers also found this effect during the optimization design. Roldán et al. [12] proposed configurations depending on the porosity in the radial and depth directions. They proposed using a set of porous slabs with different porosities as an alternative to a previous design. Chen et al. [13] investigated a double layer effect on the thermal performance of an absorber. The results indicate that the thickness of the first porous layer has a significant effect on the temperature field and pressure drop. Wang et al. systematically revealed this unique phenomenon of the porous absorber under the initial collimated irradiation [14]. We found out that the thermal performance of the absorber is significantly dependent upon the distribution of the incoming radiation on the porous media.

We propose a novel porous absorber with a variable pore structure, with a linear porosity or pore diameters distribution in the flow direction. The fluid and radiation fields will be reconstructed taking into account that the volumetric effect, the thermal performance, and the pressure-drop improvement can be carried out accordingly.

2 Model

A picture of the schematic diagram of a porous absorber with a variable pore structure medium we have proposed is shown in Fig. 1. The length in the flow direction (x) is L, and the height H in the vertical direction is assumed to be sufficient so that a one-dimensional approximation in the direction of the incoming irradiation can be invoked. We also assume that the solid matrix in the vertical direction is homogeneous and isotropic.

2.1 Local Thermal Nonequilibrium (LTNE) Model. Continuity equation

$$\frac{d\langle \rho_f u\rangle}{dx} = 0 \tag{1}$$

Momentum equation

For the one-dimensional flow, the momentum equation can be simplified to

$$\frac{d\langle P\rangle^f}{dx} = -\frac{\mu_f}{K}\langle u\rangle - \frac{\rho_f F\varphi}{\sqrt{K}}\langle u\rangle^2 \tag{2}$$

---

[1]Corresponding author.

Contributed by the Solar Energy Division of ASME for publication in the Journal of Solar Energy Engineering: Including Wind Energy and Building Energy Conservation. Manuscript received April 9, 2017; final manuscript received June 27, 2017; published online July 18, 2017. Assoc. Editor: Robert F. Boehm.

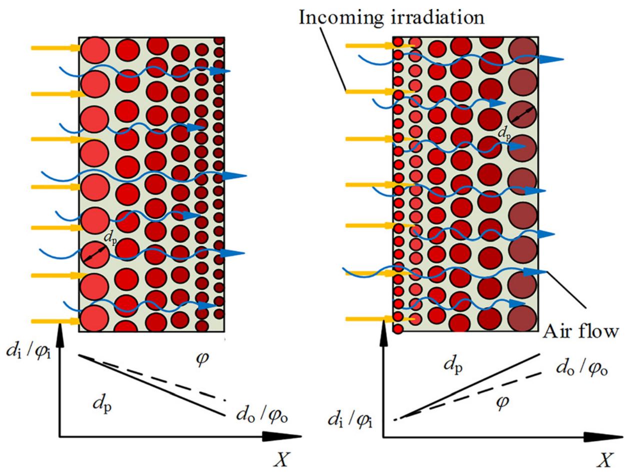

Fig. 1 Schematic for the linear distribution (*D* and *I* type layout) of the pore structure of the absorber

where $\langle P\rangle^{f}$ is the gauge pressure, and the local volume average of a quantity Φ can be defined as $\langle\Phi\rangle \equiv (1/V_f)\int_{V_f}\Phi dV$. Permeability K in the Darcy term and the empirical function F in the Forchheimer term depend primarily on the microstructure of the porous medium and can be represented as [15]

$$K = \frac{\varphi^3 d_p^2}{150(1-\varphi)^2} \tag{3}$$

$$F = \frac{1.75}{\sqrt{150\varphi^{3/2}}} \tag{4}$$

Energy equations

Fluid phases

$$(\rho c_p)_f \langle u\rangle \frac{d\langle T_f\rangle}{dx} = \frac{d}{dx}\left(\lambda_{fe}\frac{d\langle T_f\rangle}{dx}\right) + h_{sf}\alpha_{sf}(\langle T_s\rangle - \langle T_f\rangle) \tag{5}$$

Solid phases

$$0 = \frac{d}{dx}\left(\lambda_{se}\frac{d\langle T_s\rangle}{dx} - q_r\right) - h_{sf}\alpha_{sf}(\langle T_s\rangle - \langle T_f\rangle) \tag{6}$$

where the effective thermal conductivity for the fluid and solid phases is expressed as follows:

$$\lambda_{fe} = \varphi\lambda_f \tag{7}$$

$$\lambda_{se} = \varphi\lambda_s \tag{8}$$

As for the large porosity and pore diameter used in this study, the empirical correlation for the volumetric heat transfer coefficient h_v established by Hwang et al. [16] is selected and can be presented as follows:

$$h_{sf} = \left(1.064\left(\frac{\lambda_f}{d_p}\right)\mathrm{Pr}^{0.33}\mathrm{Re_d}^{0.59} + 0.004\left(\frac{d_v}{d_p}\right)^{0.35}\left(\frac{\lambda_f}{d_p}\right)\mathrm{Pr}^{0.35}\mathrm{Re_d}^{1.35}\right)\Big/2 \tag{9}$$

where d_v and α_{sf} are defined as $d_v = 4\varphi/\alpha_{sf}$, $\alpha_{sf} = 20.346(1-\varphi)\varphi^2/d_p$, and $75 < \mathrm{Re_d} < 350$.

2.2 Radiation Transfer. A modified differential approximation (P-1 model) [9] is applied to address the problem. When the incident collimated irradiation is removed from the intensity field, the remnant intensity can deviate only slightly from the isotropic condition. Similar to the classic P-1 model, we treat the remnant portion as fairly diffuse, which is the result of emission from the boundary and within the medium as well as the radiation scattered away from the collimated irradiation. We thus express the diffuse radiative flux q_d and the incident radiation G_d as follows:

$$\frac{dq_d}{dx} = \kappa\left(4\sigma\langle T_s\rangle^4 - G_d\right) + \sigma_s G_c \tag{10}$$

$$q_d = -\frac{1}{3\beta}\frac{dG_d}{dx} \tag{11}$$

Combining the expressions for q_d and G_d from Eqs. (10) and (11), the differential equation for G_d is obtained as

$$0 = \frac{1}{3\beta}\frac{d^2G_d}{dx^2} + \kappa\left(4\sigma\langle T_s\rangle^4 - G_d\right) + \sigma_s G_c \tag{12}$$

Meanwhile, q_c, the remnant collimated radiative flux after partial extinction through absorption and scattering along its path in a direction perpendicular to the boundary, is given by the exact solution

$$\mathbf{q}_c = \hat{\mathbf{s}}G_c = q_0 e^{-\tau} \tag{13}$$

where $\hat{\mathbf{s}}$ is the unit vector. The extinction coefficient β is the sum of the absorption κ and the scattering coefficients σ_s, and the initial incoming irradiation $q_c|_{x=0}$ is $1\,\mathrm{MW/m^2}$. The trend of the change of extinction coefficient can be represented as

$$\beta = \frac{\Psi}{d_p}(1-\varphi) \tag{14}$$

where the value of Ψ is a constant 3 based on the properties of reticulated porous ceramic (RPC) [17]. The expressions for the absorption and scattering coefficients are given as follows:

$$\kappa = (2-\varepsilon)\frac{3}{2d_p}(1-\varphi) \tag{15}$$

$$\sigma_s = \varepsilon\frac{3}{2d_p}(1-\varphi) \tag{16}$$

2.3 Variable Porous Structure. Considering the linear distribution of the porosity φ and pore diameter d_p in the x direction, the optical thickness τ is given by $\tau = \int_0^x \beta(x)dx$. The variation of the porosity in the x direction is defined by a linear function

$$\varphi = \varphi_i + \frac{\varphi_o - \varphi_i}{L}x \tag{17}$$

where the φ_i and φ_o are the porosity of the porous absorber at the inlet and outlet, respectively. The porosity gradient is defined as $G_p = (\varphi_o - \varphi_i)/L$. L is selected as 0.05 m, which is a typical thickness for solar absorbers. Similarly, the variable pore diameter d_p distribution in the x direction is given as

$$d_p = d_i + xG_{dp} \tag{18}$$

Thus, the derivative of the collimated irradiation q_c for the variable porosity and pore diameters can be given, respectively, as

$$\frac{dq_c}{dx} = -\beta(x) q_0 e^{-\tau} \begin{cases} \tau = \dfrac{3(1-\varphi_i)x - 1.5G_p x^2}{d_p}, & d_p = \text{const} \\ \tau = \dfrac{3(1-\varphi)}{G_{dp}} \ln\left(\dfrac{G_{dp}x + d_i}{d_i}\right), & \varphi = \text{const} \end{cases} \tag{19}$$

2.4 Boundary Conditions

2.4.1 Irradiated Surface. The entrance of the fluid flow is the irradiated surface and the only source of radiative heat loss. In the model, we disregard the effect of the porous structure on inlet fluid flow and irradiation at the boundary wall. The wall is treated as a transparent virtual surface; it is homogeneous and diffusely gray with emissivity ε_0. Under this assumption, the total incoming irradiation $\varepsilon_0 q_0$ entering the porous medium is constant. The remnant part of the incoming irradiation after absorption and scattering is treated as a volumetric phenomenon; its distribution in the incident direction can be expressed as $q_c = \varepsilon_0 q_0 e^{-\tau}$.

For the solid phase, convection on the boundary surface is included. However, the thermal radiative loss from the solid phase to the ambient is considered to be a surface phenomenon. As such, the energy balance equation is given as follows:

$$\lambda_{se} \frac{d\langle T_s\rangle}{dx}\bigg|_{x=0} = (1-\varphi)\sigma\varepsilon_0\left(\langle T_s\rangle^4\Big|_{x=0} - T_e^4\right) \tag{20}$$

For the fluid phase, the temperature of the inlet air is given by

$$T_f|_{x=0} = T_e \tag{21}$$

The diffusive radiative heat loss is considered to be emitted directly from the void space to the ambient environment. The blackbody emissive power E_b is zero when the Mashak boundary condition is applied on the virtual wall of the irradiated surface as follows:

$$\frac{1}{3\beta}\frac{dG_d}{dy}\bigg|_{x=0} = \frac{G_d|_{x=0}}{2} \tag{22}$$

2.4.2 Back Wall. It is assumed that the back wall is considered as opaque and adiabatic, the reflection there is assumed as diffuse (emissivity ε_L), consequently, the solid phase of the back wall can be considered adiabatic. In this manner, energy conservation is obtained by simultaneously considering the actual heat and fluid flow processes in the porous medium. The boundary condition for the radiative heat transfer based on the previously cited assumption can be written as follows:

$$-\frac{1}{3\beta}\frac{dG_d}{dx}\bigg|_{x=L} = \frac{\varepsilon_1\left(4\sigma_s\langle T_s\rangle^4|_{x=L} - G_d|_{x=L}\right) + 4(1-\varepsilon_L)H_c}{2(2-\varepsilon_L)} \tag{23}$$

where H_c is the collimated radiative flux arriving at the back wall $q_c|_{x=L}$, and the emissivity of the two boundaries (ε_0 and ε_L) is set as a constant 0.8. For the solid phase, the impinging collimated irradiation can be coupled by the following boundary condition:

$$-\lambda_{se}\frac{d\langle T_s\rangle}{dx}\bigg|_{x=L} - \frac{1}{3\beta}\frac{dG_d}{dx}\bigg|_{x=L} + H_c = 0 \tag{24}$$

The related dimensionless parameters can be defined as follows:

$$X = \frac{x}{L} \tag{25}$$

$$\theta_f = \frac{T_f}{T_e} \tag{26}$$

$$\theta_s = \frac{T_s}{T_e} \tag{27}$$

where L is the thickness of the porous medium, and $T_e = 300\,\text{K}$ is the ambient temperature. The conductive heat flux for the solid phase Ψ_s can be represented as

$$\Psi_s = -\frac{\lambda_{se}}{q_0}\frac{d\langle T_s\rangle}{\partial x} \tag{28}$$

and the diffuse radiative flux Ψ_d and the collimated radiative flux Ψ_c can be represented as follows:

$$\Psi_d = -\frac{1}{3\beta q_0}\frac{dG_d}{\partial x} \tag{29}$$

$$\Psi_c = G_c/q_0 \tag{30}$$

For air, the thermal properties are fitted to data from Ref. [18] for the temperatures between 100 K and 2000 K. For the density ρ_f, the heat capacity c_p, and the dynamic viscosity η_f, the correlations are

$$\rho_f = 1.82161 - 0.002965 \cdot T_f + 0.00000151652 \cdot T_f^2 \tag{31}$$

$$C_p = 1038.1 - 0.310926 \cdot T_f + 0.000762955 \cdot T_f^2 + 3.4915 \times 10^{-7} \cdot T_f^3 \tag{32}$$

$$\eta_f = -8.38 \times 10^{-7} + 8.36 \times 10^{-8} \cdot T_f - 7.69429583 \times 10^{-11} \cdot T_f^2 + 4.6437266 \times 10^{-14} \cdot T_f^3 - 1.06585607 \times 10^{-17} \cdot T_f^4 \tag{33}$$

2.5 Numerical Procedure and Validation. Governing equations are discretized using a SIMPLE algorithm by applying the finite volume method. An upwind differencing method is employed to discretize the convective terms. Convergence is considered to have been reached when the relative variation of temperature between consecutive iterations is smaller than 10^{-8} for all the grid points in the computational domain after the grid independent test. The numerical method for the P-1 approximation and its validation on the radiation transfer have been well established in our previous work [9].

3 Results and Discussion

3.1 Effects of the Variable Porosity Distribution. Figures 2(*a*) and 2(*b*) show the effect of the variable porosity layout on the temperature and heat flux fields along the X axis. The comparison between the increasing layout ($\varphi = 0.5$–0.9) (I type), decreasing layout ($\varphi = 0.9$–0.5) (D type), and the constant layout, which we refer to as C type porosity layout, is shown in Fig. 2(*a*). We define the average porosity as $\varphi_a = (\varphi_i + \varphi_o)/2$. The comparison is based on the same $\varphi_a = 0.7$ and a 2 mm pore diameter. The dimensionless temperature distribution shows that the D type layout is better than the I type layout by decreasing the solid temperature at the irradiated surface.

The distribution of the conductive heat flux (Ψ_s) in the solid phase is shown in Fig. 2(*b*). It is obvious that Ψ_s is negative (pointing from the back wall to the irradiated surface) at the irradiated side. Its absolute value on the X axis gradually reduces to zero and then increases, leading to the creation of a zero-value point that clearly corresponds to the maximum temperature point located inside, rather than on, the irradiated surface, thus moving

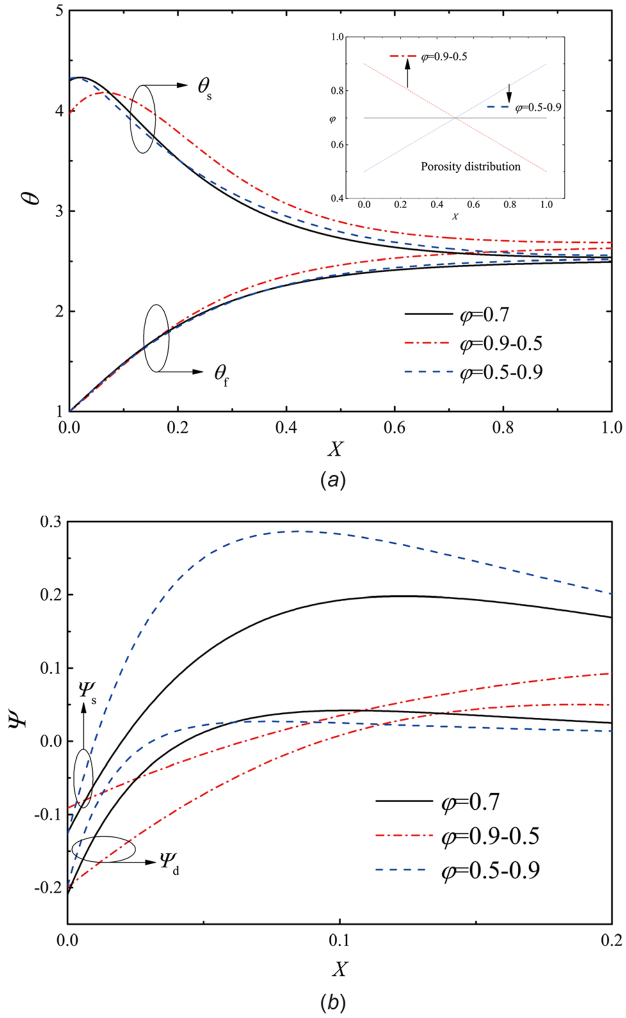

Fig. 2 Comparison between the *I* and *D* type porosity layout on the temperature and heat flux fields along the *X* axis: (*a*) dimensionless temperature θ and (*b*) dimensionless heat flux Ψ ($d_p = 2$ mm and $q_0 = 1$ MW/m^2)

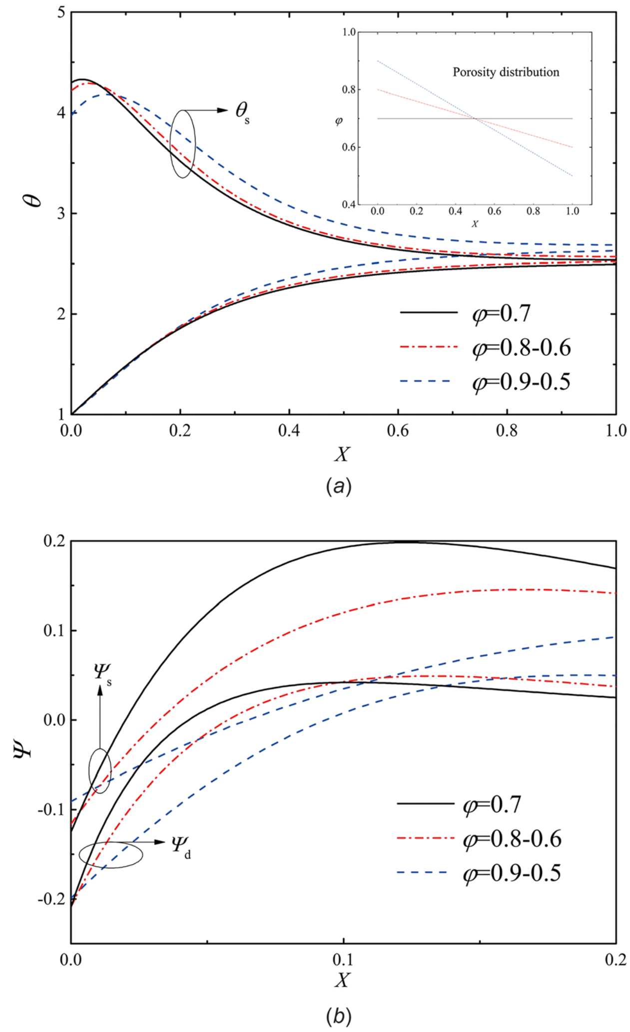

Fig. 3 Effect of the porosity distribution gradient on the temperature and heat flux fields along the *X* axis: (*a*) dimensionless temperature θ and (*b*) dimensionless heat flux Ψ ($d_p = 2$ mm and $q_0 = 1$ MW/m^2)

the maximum solid temperature inside the porous medium due to the volumetric effect. It then converges to zero quickly, hence, the dimensionless length X is shown only before 0.2 in Fig. 2(*b*). For the *D* type layout ($\varphi = 0.9$–0.5), the volumetric effect is enhanced, and the incoming irradiation can penetrate deeply into the porous medium compared to the *I* type. Hence, the maximum temperature point is put forward into the absorber. Consequently, a lower solid temperature at the irradiated surface is achieved.

Since the *D* type layout is better than the *I* type, two *D* type porosity layouts ($\varphi = 0.8 \sim 0.6$ and $\varphi = 0.9$–0.5 are compared for the same average porosity $\varphi = 0.7$ It can be seen in Fig. 3(*a*) that the larger the gradient of the φ distribution, the lower the solid temperature θ_s at the irradiated surface, resulting in a larger outlet fluid temperature θ_f. In the absorber, the larger gradient porosity distribution results in less conductive heat loss and diffusive radiative loss at the irradiated surface (see Ψ_s and Ψ_d in Fig. 3(*b*)), which is beneficial for decreasing the total heat loss of the absorber.

With the same porosity φ_i at the irradiated surface, the effect of the porosity at the back side (φ_o) of the absorber on the temperature distribution is also analyzed in Figs. 4(*a*) and 4(*b*). Three different values of φ_o were selected ($\varphi_o = 0.45$, $\varphi_o = 0.7$, and $\varphi_o = 0.8$) as can be seen in Fig. 4(*a*). The dimensionless temperature distributions of the fluid phase θ_f and the solid phase θ_s are also shown in Fig. 4(*a*). The temperature gradients are similar to each other at the irradiated surface because of the same value of φ_i. However, with an increase in the value of φ_o, the outlet fluid temperature on the back side increases. That is, with a larger inlet porosity ($\varphi_i > 0.8$), the larger φ_o is, the higher the thermal efficiency will be.

Figure 4(*b*) shows the distribution of the conductive heat flux Ψ_s and the radiative heat flux Ψ_d in the solid phase. Both conductive and radiative heat fluxes attenuate to zero at the back side of the absorber, which shows that the selection for the thickness of the absorber is appropriate. Before the "crossing point" (see the green point near $X = 0.1$) near the irradiated side of the absorber, there is a larger porosity gradient resulting in a more compact pore structure, hence the absolute value of the Ψ_s, i.e., the direct radiative losses are larger.

3.2 Effect of Variable Pore Size Distribution. The effect of a variable pore diameter distribution on the energy transport and the pressure drop is different than that of the porosity due to different heat transfer and radiation properties. Consequently, an analysis was carried out based on different pore diameter distributions: *D* type ($d_p = 3$–1 mm), *I* type ($d_p = 1$–3 mm), and *C* type ($d_p = 2$ mm) layouts (Fig. 5). The premise of the comparison is that the average pore diameter is a constant $d_a = 2$ mm ($d_a = (d_i + d_o)/2$) with the same porosity $\varphi = 0.9$. The dimensionless temperature distribution shows that *D* type is better than the *I*

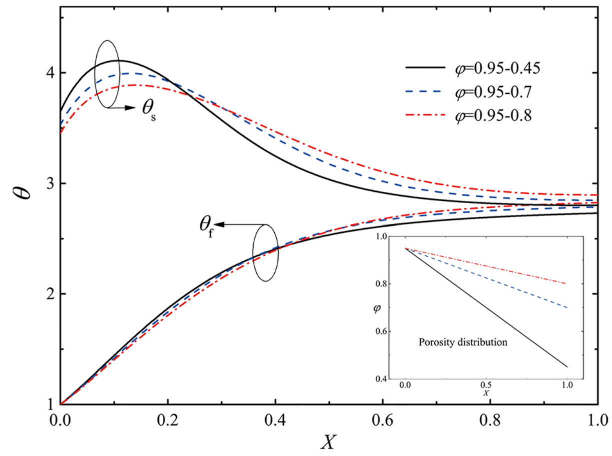

(*a*)

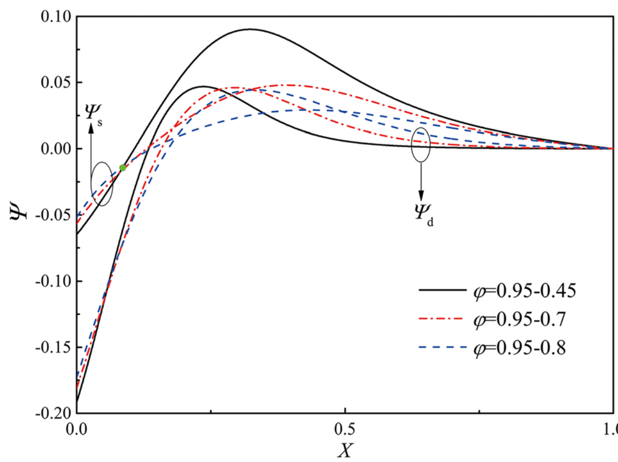

(*b*)

Fig. 4 Effect of φ_o on the temperature and heat flux distributions along the *X* axis under *D* type porosity layout: (*a*) dimensionless temperature θ and (*b*) dimensionless heat flux Ψ ($d_p = 2$ mm and $q_0 = 1$ MW/m^2) (see color figure online)

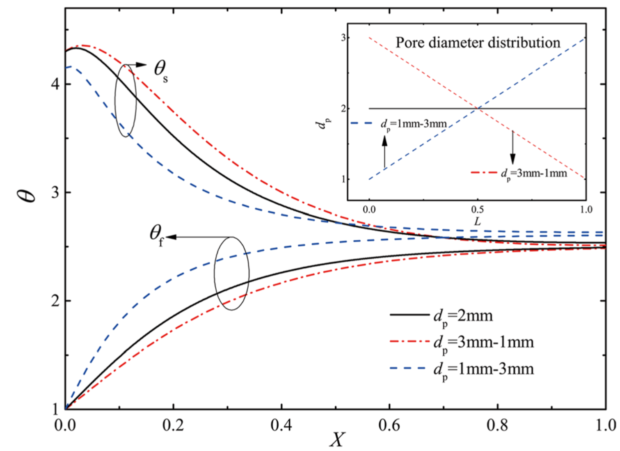

(*a*)

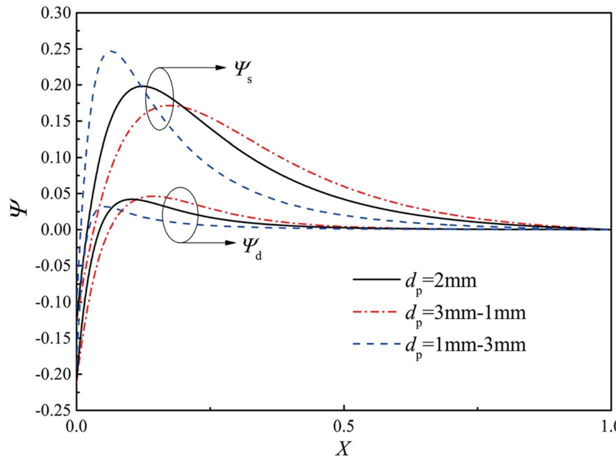

(*b*)

Fig. 5 Comparison between the *I* and *D* type pore diameter layout on the temperature and heat flux fields along the *X* axis: (*a*) dimensionless temperature θ and (*b*) dimensionless heat flux Ψ ($\varphi = 0.7$ and $q_0 = 1$ MW/m^2)

type. The difference in the dimensionless outlet air temperatures between the *D* and *I* type is nearly 50 K, which shows that the variable distribution has a significant effect on the thermal performance.

The distribution of conductive heat flux Ψ_s and radiative heat flux Ψ_d in the solid phases is also given in Fig. 5(*b*). For the *I* type layout, the volumetric effect is weakened at the irradiated side. In this case, the heat transfer between the solid and fluid phases is enhanced due to the compact pore structure at the irradiated side. Considering the solid section area is constant under the same porosity between the two types of layouts, the absolute values of Ψ_s and Ψ_d near the irradiated surface for the *I* type are very close but slightly lower than that of the *D* type. Combined with the earlier results, the *D* type porosity layout simultaneously with the *I* type pore layout would be an excellent pore structure for energy transport along the *X* axis of the porous absorber.

Since the *I* type is better than the *D* type, three different pore diameters at the back side of the absorber are selected: $d_o = 1$ mm, 2 mm, and 3 mm. With the same pore diameter at the irradiated surface ($d_i = 0.5$ mm), the effect of d_o on the dimensionless temperature distribution is displayed in Figs. 6(*a*) and 6(*b*). The temperature distributions are similar to each other because of the same d_i at the irradiated surface. However, with a decrease in the value of d_o, the outlet fluid temperature at the back side increases, which is due to the smaller average value of d_p. As such, the interphase convection is enhanced, which is beneficial for improving the thermal performance of the absorber. The variable pore diameter influences the energy transport by a different mechanism than that of the variable porosity. That is, the former has a greater effect on the conductive heat flux Ψ_s, as compared to the radiative heat flux Ψ_d.

4 Conclusions

A modeling work that considers the continuous linear porosity or pore diameter distribution is presented to develop a novel porous absorber with a variable pore structure. Three typical distribution layouts which were analyzed, included the *I*, *D*, and *C* types. The mechanisms for convective and radiative transport considering the variable pore structure distribution were discussed in detail.

The *D* type porosity distribution is better than the *I* type. Due to the enhanced volumetric effect, the incoming irradiation can penetrate deeper into the porous medium compared with the *I* type. Consequently, a lower solid temperature at the irradiated surface is achieved. The variable pore diameter influences the energy transport by a different mechanism than the variable porosity. The variable pore diameter has a greater effect on the distribution of conductive heat flux Ψ_s in the solid phase than the radiative heat flux Ψ_d. Comprehensively, the *D* type porosity layout combined

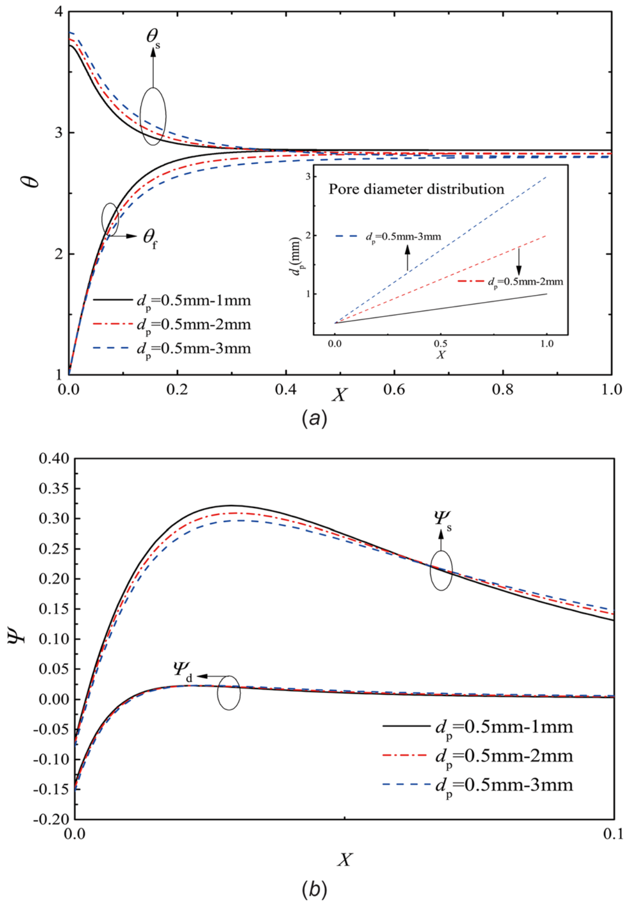

Fig. 6 Effect of d_o on the temperature and heat flux distributions along the X axis under the I type pore diameter layout: (a) dimensionless temperature θ and (b) dimensionless heat flux Ψ ($\varphi = 0.7$ and $q_0 = 1$ MW/m^2)

with the I type pore distribution would be an excellent pore structure layout for a porous absorber.

Due to the absence of experimental correlations, one of the φ and d_p values is set to be a constant when the other one is considered to be a variable. The combination of these two parameters can be further analyzed and more detailed information of the energy transport can be revealed at a pore-scale level analysis focused on this variable pore structure.

Acknowledgment

The support of the National Natural Science Foundation of China (No. 51509076), Natural Science Foundation of Jiangsu Province (No. BK20150816), and Fundamental Research Fund for Central Universities under Project No. (2017B13814) is acknowledged. The authors also gratefully acknowledge the financial support from the National Basic Research Program (973 Program, No. 2010CB227102) of Chinese Science and Technology Department.

Nomenclature

c_p = specific heat of fluid at constant pressure (J kg^{-1} K^{-1})
d_p = pore diameter (m)
F = inertial coefficient
G = incident radiation/gradient
h_{sf} = fluid-to-solid heat transfer coefficient (W m^{-2} K)
K = permeability (m^2)
L = thickness of a absorber (m)
P = pressure (Pa)
Pr = Prandtl number
q = heat flux
q_0 = initial heat flux (W/m^{-2})
$\hat{\mathbf{s}}$ = unit vector in the direction of the fluid flow
T = temperature (K)
u = velocity (m/s)
$\mathbf{V}$ = velocity vector (m s^{-1})

Greek Symbols

α_{sf} = specific surface area of the porous medium (m^{-1})
β = extinction coefficient (m^{-1})
ε = emissivity
ζ = ratio of solid to fluid thermal conductivities
θ = dimensionless temperature
λ = thermal conductivity (W m^{-1} K^{-1})
μ = dynamic viscosity (kg m^{-1} s^{-1})
ρ = density (kg m^{-3})
σ = Stefan–Boltzmann constant
σ_s = scattering coefficient
τ = optical thickness
φ = porosity
Ψ = dimensionless heat flux
ω = single scattering albedo

Subscripts

a = average
c = collimated
d = diffuse/pore diameter
e = effective/environment
f = fluid phase
i = inlet
o = outlet
s = solid phase

References

[1] Daabo, A. M., Mahmoud, S., and Al-Dadah, R. K., 2016, "The Optical Efficiency of Three Different Geometries of a Small Scale Cavity Receiver for Concentrated Solar Applications," Appl. Energy, **179**, pp. 1081–1096.
[2] Ho, C. K., and Iverson, B. D., 2014, "Review of High-Temperature Central Receiver Designs for Concentrating Solar Power," Renewable Sustainable Energy Rev., **29**, pp. 835–846.
[3] Roldán, M. I., Zarza, E., and Casas, J. L., 2015, "Modelling and Testing of a Solar-Receiver System Applied to High-Temperature Processes," Renewable Energy, **76**, pp. 608–618.
[4] Roldán, M. I., Fernández-Reche, J., and Ballestrín, J., 2016, "Computational Fluid Dynamics Evaluation of the Operating Conditions for a Volumetric Receiver Installed in a Solar Tower," Energy, **94**, pp. 844–856.
[5] Cheng, Z. D., He, Y. L., and Cui, F. Q., 2013, "A New Modelling Method and Unified Code With MCRT for Concentrating Solar Collectors and Its Applications," Appl. Energy, **101**, pp. 686–698.
[6] Chen, X., Xia, X.-L., Dong, X.-H., and Dai, G.-L., 2015, "Integrated Analysis on the Volumetric Absorption Characteristics and Optical Performance for a Porous Media Receiver," Energy Convers. Manage., **105**, pp. 562–569.
[7] Fend, T., Schwarzbözl, P., Smirnova, O., Schöllgen, D., and Jakob, C., 2013, "Numerical Investigation of Flow and Heat Transfer in a Volumetric Solar Receiver," Renewable Energy, **60**, pp. 655–661.
[8] Aichmayer, L., Spelling, J., and Laumert, B., 2015, "Preliminary Design and Analysis of a Novel Solar Receiver for a Micro Gas-Turbine Based Solar Dish System," Sol. Energy, **114**, pp. 378–396.
[9] Wang, P., Vafai, K., Liu, D. Y., and Xu, C., 2015, "Analysis of Collimated Irradiation Under Local Thermal Non-Equilibrium Condition in a Packed Bed," Int. J. Heat Mass Transfer, **80**, pp. 789–801.
[10] Wang, P., Liu, D. Y., Xu, C., Xia, L., and Zhou, L., 2016, "A Unified Heat Transfer Model in a Pressurized Volumetric Solar Receivers," Renewable Energy, **99**, pp. 663–672.
[11] Wang, P., Li, J. B., Bai, F. W., Liu, D. Y., Xu, C., Zhao, L., and Wang, Z. F., 2017, "Experimental and Theoretical Evaluation on the Thermal Performance of a Windowed Volumetric Solar Receiver," Energy, **119**, pp. 652–661.

[12] Roldán, M. I., Smirnova, O., Fend, T., Casas, J. L., and Zarza, E., 2014, "Thermal Analysis and Design of a Volumetric Solar Absorber Depending on the Porosity," Renewable Energy, **62**(3), pp. 116–128.
[13] Chen, X., Xia, X.-L., Meng, X.-L., and Dong, X.-H., 2015, "Thermal Performance Analysis on a Volumetric Solar Receiver With Double-Layer Ceramic Foam," Energy Convers. Manage., **97**, pp. 282–289.
[14] Wang, P., Vafai, K., and Liu, D. Y., 2016, "Analysis of the Volumetric Phenomenon in Porous Beds Subject to Irradiation," Numer. Heat Transfer, Part A, **70**(6), pp. 567–580.
[15] Alazmi, B., and Vafai, K., 2000, "Analysis of Variants Within the Porous Media Transport Models," ASME J. Heat Transfer, **122**(2), pp. 303–326.
[16] Hwang, G. J., Wu, C. C., and Chao, C. H., 1995, "Investigation of Non-Darcian Forced Convection in an Asymmetrically Heated Sintered Porous Channel," ASME J. Heat Transfer, **117**(3), pp. 725–732.
[17] Hendricks, T. J., and Howell, J. R., 1996, "Absorption/Scattering Coefficients and Scattering Phase Functions in Reticulated Porous Ceramics," ASME J. Heat Transfer, **118**(1), pp. 79–87.
[18] Lemmon, E. W., Jacobsen, R. T., Penoncello, S. G., and Friend, D. G., 2000, "Thermodynamic Properties of Air and Mixtures of Nitrogen, Argon, and Oxygen From 60 to 2000 K at Pressures to 2000 MPa," J. Phys. Chem. Ref. Data, **29**(3), pp. 331–385.